Combustion and Flame 158 (2011) 57–68

Contents lists available at ScienceDirect

Combustion and Flame

journal homepage: www.elsevier.com/locate/combustflame

Gas-phase saturation and evaporative cooling effects during wet compression of a fuel aerosol under RCM conditions

S.S. Goldsborough [a,*], M.V. Johnson [b,1], G.S. Zhu [c,2], S.K. Aggarwal [d,3]

[a] Department of Mechanical Engineering, Marquette University, PO Box 1881, Milwaukee, WI 53201-1881, USA
[b] Energy Systems Division, Argonne National Laboratory, 9700 S. Cass Avenue, Argonne, IL 60439-4815, USA
[c] HDEP Performance & Emissions, DTNA – Detroit Diesel Corporation, 13400 Outer Dr. West, Detroit, MI 48239, USA
[d] Department of Mechanical and Industrial Engineering, University of Illinois at Chicago, 1030 Engineering Research Facility, 842 W. Taylor Street, Chicago, IL 60607, USA

ARTICLE INFO

Article history:
Received 18 April 2010
Received in revised form 20 May 2010
Accepted 18 July 2010
Available online 13 August 2010

Keywords:
Wet compression
Droplet evaporation
Aerosol RCM
Transient model

ABSTRACT

Wet compression of a fuel aerosol has been proposed as a means of creating gas-phase mixtures of involatile diesel-representative fuels and oxidizer + diluent gases for rapid compression machine (RCM) experiments. The use of high concentration aerosols (e.g., ~0.1 mL_{fuel}/L_{gas}, ~1×10^9 droplets/L_{gas} for stoichiometric fuel loading at ambient conditions) can result in droplet–droplet interactions which lead to significant gas-phase fuel saturation and evaporative cooling during the volumetric compression process. In addition, localized stratification (i.e., on the droplet scale) of the fuel vapor and of temperature can lead to non-homogeneous reaction and heat release processes – features which could prevent adequate segregation of the underlying chemical kinetic rates from rates of physical transport. These characteristics are dependent on many factors including physical parameters such as overall fuel loading and initial droplet size relative to the compression rate, as well as fuel and diluent properties such as the boiling curve, vaporization enthalpy, heat capacity, and mass and thermal diffusivities. This study investigates the physical issues, especially fuel saturation and evaporative cooling effects, using a spherically-symmetric, single-droplet wet compression model. *n*-Dodecane is used as the fuel with the gas containing 21% O_2 and 79% N_2. An overall compression time and compression ratio of 15.3 ms and 13.4 are used, respectively. It is found that smaller droplets ($d_0 \sim 2$–3 μm) are more affected by 'far-field' saturation and cooling effects, while larger droplets ($d_0 \sim 14$ μm) result in greater localized stratification of the gas-phase due to the larger diffusion distances for heat and mass transport. Vaporization of larger droplets is more affected by the volumetric compression process since evaporation requires more time to be completed even at the same overall fuel loading. All of the cases explored here yield greater compositional stratification than thermal stratification due to the high Lewis numbers of the fuel–air mixtures ($Le_g \sim 3.8$).

1. Introduction

Wet compression is the process whereby vaporization is achieved via compression heating of the gas-phase of a droplet laden aerosol. This phenomenon has received increasing attention in the power generation field in recent years with applications to advanced combustion processes and alternative fuel formulations in internal combustion engines [1–7], and to continuous cooling configurations using water aerosols in gas turbine engines [8–10]. In shock tubes (STs) and rapid compression machines (RCMs) wet compression has also been proposed as a means of preparing test gases for high molecular weight, involatile liquid fuels relevant to the transportation industry. Traditional charge preparation techniques for these laboratory apparatuses generally use external mixing protocols based on partial pressure methodologies [11,12]. Diesel-representative fuels however, have very low vapor pressures at standard conditions (e.g., $P^{sat} < 1$ Torr) which make this option difficult or impossible. Heating the mixing tanks and test apparatus can lead to better fuel vaporization but this is still limited in RCMs due to seal degradation issues, and there is concern for pre-test reactivity during the mixture preparation process. Aerosols of suspended fuel droplets ($d_{mean} \sim 8$–18 μm) have been used to deliver liquid fuels to the devices where subsequent volumetric compression of the surrounding gas-phase leads to evaporation of the liquid fuel droplets [13,14]. In shock tubes where test temperatures generally range from 900 to 2000 K the gas-phase compression event is achieved via a rapidly traveling shock wave ($\Delta t_{comp} \sim 30$ μs; $T_{comp} \sim 600$–700 K); the passing of the initial wave not only

* Corresponding author. Fax: +1 414 288 7790.
E-mail address: scott.goldsborough@mu.edu (S.S. Goldsborough).
[1] Fax: +1 630 252 3443.
[2] Fax: +1 313 592 5906.
[3] Fax: +1 312 413 0447.

0010-2180/$ - see front matter © 2010 The Combustion Institute. Published by Elsevier Inc. All rights reserved.
doi:10.1016/j.combustflame.2010.07.018

Nomenclature

Roman

c_p	specific heat at constant pressure
c_v	specific heat at constant volume
D	mass diffusion coefficient
d	diameter
h	specific enthalpy
I	specific internal energy
Kn	Knudsen number (η/r_s)
L	heat of vaporization
Le	Lewis number (κ/D)
$\dot{m}$	net evaporation rate
m''	net evaporation flux
$\bar{m}$	non-dimensional evaporation rate, $\dot{m}/4\pi\rho_g D_g r_s$
N	total number of species in the mixture
P	pressure
r	radial direction
R	ideal gas constant
t	time
$\bar{t}$	non-dimensional time, $\int \hat{\kappa}\, dt/r_s^2$
T	temperature
u	radial velocity
V	volume
X	mass fraction, liquid-phase
Y	mass fraction, vapor phase
z	compressibility factor

Greek

α	thermal conductivity
γ	ratio of specific heats, c_p/c_v
ζ	thickness of free-molecular flow region
η	mean free path
φ	equivalence ratio
κ	heat diffusivity
λ	second viscosity coefficient
μ	dynamic viscosity
ρ	density
υ	specific volume
ϕ	fugacity coefficient

Subscripts

a	air
f	fuel
g	gas-phase
ii	iith cell
j	jth species
k	kth species
l	liquid-phase
s	droplet surface
0	initial value
∞	'far-field' value

increases the pressure and temperature of the surrounding bath gases but it fragments the initial droplets and results in high convective velocities near the droplet surface (which enhances vaporization). The subsequent reflected wave compresses the evaporated fuel + oxidizer + diluent mixture to the test conditions. In RCMs, where test temperatures range from 600 to 1100 K, the compression event is much slower (e.g., $\Delta t_{comp} \sim 15$–60 ms) and bulk gas (i.e., on the scale of the reaction chamber) fluid dynamics are often suppressed in order to minimize unwanted heat loss during the test period [15]. Droplet evaporation is therefore much slower and is generally constrained by the initial droplet size and ensuing gas-phase diffusion processes. Evaporation must also be achieved at lower temperatures than in STs (e.g., by ~500 K to precede low temperature chemical reactivity).

The design and operation of aerosol RCMs which can effectively utilize the wet compression process for involatile diesel-representative fuels requires a fundamental understanding of droplet evaporation including both near-droplet and 'far-field' processes. This study builds upon previous work to develop an integrated simulation tool and investigates important issues for aerosol RCM applications. In a previous study using an isolated droplet (i.e., $\varphi \sim 0.0$) we found that shorter compression times can lead to greater gas-phase stratification, in both composition and temperature due to the non-linear rate of temperature, and thus saturation pressure rise with volumetric compression (as seen shortly in Fig. 2), and the relatively slower diffusion of mass from and heat to the droplet. In addition, it was found that lower gas pressures can enhance evaporation during wet compression because the gas-phase fuel mass fraction at the droplet surface is higher and this increases the rate of diffusive transport of fuel away from the droplet.

The use of high aerosol concentrations (e.g., ~0.1 mL_{fuel}/L_{gas}, corresponding to $\sim 1 \times 10^9$ droplets/L_{gas}), is necessary to achieve desired fuel loadings in order to investigate engine relevant chemistry (e.g., φ = 0.5–2.0, 5–21% O_2, P_{comp} = 10–50 bar). This condition can result however in droplet–droplet interactions such that significant gas-phase fuel saturation and evaporative cooling occurs during the piston compression process. This can alter the rate of evaporation and the extent of volumetric compression required to achieve complete vaporization. In addition, localized stratification (i.e., on the droplet scale) of the fuel vapor and of temperature can occur due to insufficient rates of transport; this could lead to non-homogeneous reaction and heat release processes – features which may not enable an adequate segregation of the chemical kinetic rates from rates of physical transport. These characteristics are dependent on many factors including physical parameters such as overall fuel loading and initial droplet size relative to the compression rate, as well as fuel and diluent properties including the fuel's boiling curve, vaporization enthalpy, heat capacity, molar densities, and mass and thermal diffusivities.

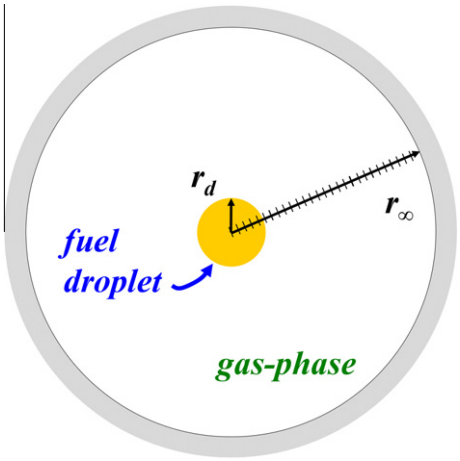

Fig. 1. Schematic of the wet compression model illustrating liquid- and gas-phase domains and the location of the 'far-field' boundary.

The objective of this study is to investigate the physical parameters in order to better understand the factors which influence wet compression; this information can then be used towards the design

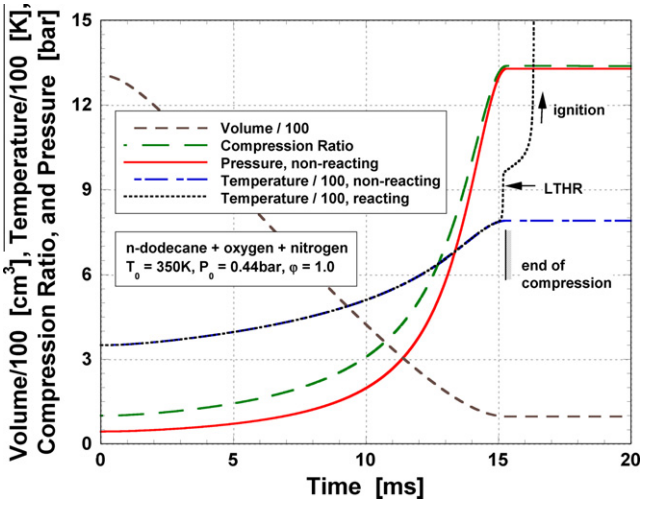

Fig. 2. Representative volume, compression ratio, temperature and pressure histories used in this study where the volume data is typical of rapid compression machines described in the literature. The temperature and pressure trajectories are computed assuming an adiabatic compression process from $T_0 = 350$ K and $P_0 = 0.44$ bar, respectively, with $\varphi = 1.0$ using a fully pre-vaporized/pre-mixed charge. Non-reacting and reacting temperature profiles are shown where the reacting case is computed based on the detailed kinetic mechanism of Westbrook et al. [27].

of successful aerosol RCMs. A spherically-symmetric, single-droplet wet compression model is used in this study where *n*-dodecane is considered as the fuel while the gas-phase is considered to be air (21% O_2, 79% N_2). A range of initial droplet diameters from $d_0 = 2$ to 14 μm is covered with fuel loadings from $\varphi = 0.5$ to 2.0. A compression time and extent of compression (i.e., maximum compression ratio, $CR_{max} = V_0/V_{min}$) that are representative of typical RCMs are used. The remainder of this paper is organized as follows. First, an overview of the wet compression model is presented along with a brief discussion of modifications undertaken for this study. Simulation results are then presented covering the range of initial droplets sizes and various fuel loadings. Differences in the evaporation behavior and the gas-phase transport for the different cases are highlighted and discussed. Finally, issues regarding successful design and operation of an aerosol RCM are discussed.

2. Model

This study utilizes the wet compression model described previously by Johnson et al. [16]. The model integrates a fully transient evaporation model developed by Aggarwal and co-workers [17–19] with a gas-phase volumetric compression model. The evaporation sub-model employs a continuum formulation with phase and thermal equilibria prescribed at the liquid–vapor interface. This prescription can lead to errors in the predicted evaporation times for the droplets investigated here due to gas kinetic effects at small droplet diameters (e.g., $d_0 < 5$ μm). However, these errors appear to be modest (~5–15%) and the trends in the modeling results using the interface equilibria prescription appear to be comparable to those observed with a refined modeling approach where gas kinetic effects are taken into account (e.g., see Appendix A, as well as Refs. [20–23]). The droplet and surrounding gas-phase are assumed to be spherically-symmetric, and thermal and concentration gradients within the droplet are taken into account. Absorption of the oxidizer and diluent gas into the liquid-phase is also considered. The droplet sizes used in this study are small enough, however, so that no internal stratification is seen. No bulk gas velocity is used (i.e., the Reynolds number is assumed to be zero), as this provides a useful lower bound for the rate of transport of fuel and energy to and from the 'far-field', and the resulting localized compositional and thermal stratification. Spatial variations in pressure are taken into account in the model, as are variations in the liquid- and gas-phase properties due to the large changes in temperature and pressure experienced under some conditions. (For all of the cases explored in this study however, the pressure is found to be spatially uniform.) Real gas equations of state (e.g., Peng-Robinson) are facilitated in the software, although the compressibility factors ($z = P/\rho RT$) for all of the cases explored here are found to be nearly 1.0 so that the ideal gas model could be reasonably used. A mesh compression operation is integrated with the evaporation model in order to simulate the gas-phase compression heating process. This sub-model accounts for the induced convective radial flow towards the droplet due to volumetric compression. The evaporation sub-model has been detailed previously in Refs. [17–19] where predictions are validated against a range of experimental data. Application of the integrated model to study wet compression of an isolated droplet has been described in Ref. [16]; however there is currently a lack of experimental data for validation of the integrated wet compression model. In Ref. [16] other approaches for modeling wet compression are reviewed and compared. It was demonstrated in that work that simplified models, such as quasi-steady formulations, result in significant discrepancies (e.g., +50% in total evaporation time) compared to the results predicted with the fully transient formulation used here.

Table 1
Geometric constraints of the computational mesh used to specify fuel loadings for *n*-dodecane and air mixtures at $T_0 = 350$ K, $P_0 = 1$ bar and $\rho_{l,0} = 0.734$ g/cm^3.

φ	$r_{\infty,0}/r_{s,0}$
0.0	460
0.5	28.2
1.0	22.5
2.0	17.7

The wet compression model is modified from Ref. [16] in order to investigate droplet–droplet interactions, especially fuel saturation and evaporative cooling effects under RCM conditions. Figure 1 illustrates the configuration implemented in the model for this study. A single droplet is used to represent the fuel loaded into the RCM for an experiment while the gas-phase domain is constrained in order to represent the finite volume of the RCM device. It is assumed that the aerosol is mono-dispersed and uniformly distributed throughout the reaction chamber volume. No-flux (i.e., no-gradient) boundary conditions are applied at the edge of the gas-phase domain (i.e., the 'far-field') to ensure that mass, momentum, energy and species cannot enter or leave the reaction chamber volume (i.e., $\partial\rho_{k,\infty}/\partial r = 0$, $\partial\rho_{\infty}/\partial r = 0$, $u_{\infty} = 0$, and $\partial T_{\infty}/\partial r = 0$ at $r = r_{\infty}$). The overall fuel–air ratio for the simulation is specified according to the equivalence ratio definition

$$\varphi = \frac{(m_f/m_a)}{(m_f/m_s)_{\text{stoich}}} = \frac{1}{0.067}\frac{\rho_{f,0} r_{d,0}^3}{\rho_{a,0}(r_{\infty,0}^0 - r_{d,0}^3)} \quad (1)$$

where the subscripts '*f*' and '*a*' refer to fuel and air, respectively, and the subscript '0' indicates the initial conditions. The value of 0.067 in this expression represents the stoichiometric fuel–air ratio for *n*-dodecane ($(m_f/m_a)_{\text{stoich}}$). The initial densities of the fuel and air are dependent on the initial temperature and pressure during the experiment; once these are specified along with the initial droplet diameter, the initial 'far-field' boundary used in the simulation is located. Table 1 lists the geometric parameters used in this study where a range of equivalence ratios typical for RCM experiments

is covered. It can be seen here that larger values of φ require smaller gas volumes for the same droplet size, while large droplet sizes require greater 'far-field' distances for the same fuel loading.

The time-varying location of the 'far-field' boundary, which governs the rate of compression heating, is dependent on the volumetric history of the RCM. This is expressed using the time-varying compression ratio as expressed in

$$CR(t) = \frac{V_0}{V(t)} = \frac{r_{\infty,0}^3}{r_\infty^3(t)} \quad (2)$$

For this work we have used $CR(t)$ as an input table where the time history is representative of the operational characteristics of RCMs currently utilized for chemical kinetic studies [14,15,24,25].

More details of the wet compression model, including the governing equations, a summary of the thermo-physical models used for this study, and issues associated with thermodynamic non-equilibrium at the droplet surface can be found in Appendix A. While this study is focused on features important for successful aerosol RCM operation, the model has applicability to broader topics such as those listed in the previous section.

3. Model results

The results presented here are for an *n*-dodecane droplet evaporating into air; the air is assumed to be composed of 79% nitrogen and 21% oxygen. *n*-Dodecane is a very low volatility (P^{sat} < 1 Torr, T_{boil} = 488 K @ STP) normal alkane that has been used as a single component surrogate to represent the fundamental features of diesel fuel ignition. It has also been used as a test component for the design and validation of the aerosol ST concept [13]. It was selected for this study in order to better understand the features of wet compression as it might be applied within an aerosol RCM. A companion study [26] investigates fuels with different boiling curve and transport characteristics, as well as diluent gases which have different thermo-physical properties from nitrogen. Experimental data for ρ, c_p, etc. for *n*-dodecane has been reviewed in Ref. [16] where these data are compared to the thermo-physical models used in this study; excellent agreement is seen across all of the experimental data. Additionally, in a previous study, the computational model has been extensively validated for the transient evaporation of an *n*-heptane droplet under high pressure conditions [17]. For most of the simulations conducted here the droplet and gas-phase are assumed to be initially in thermal and mechanical equilibrium (i.e., uniform temperature and pressure throughout), with the liquid-phase containing only *n*-dodecane and the gas-phase only air. For select runs presented in Figs. 5 and 6 the simulations are initialized using a saturated condition, meaning the gas-phase is assumed to contain *n*-dodecane uniformly distributed at its saturation pressure. The starting temperature and pressure for these cases are determined based on the extent of evaporative cooling that would occur to achieve this level of vaporization. This may be a more realistic starting condition for an aerosol that is generated upstream of the RCM where there would be sufficient residence time within the delivery manifold that some pre-compression evaporation occurs.

A piston trajectory for a typical RCM is used to specify the time-varying volume of the gas-phase computational mesh. The trajectory is representative of designs discussed in recent literature with compression times on the order of 15–25 ms and compression ratios ranging from 11 to 25 [14,15,24,25]. The piston trajectory has been normalized so that any maximum compression ratio, $CR_{max} = V_0/V_{min}$, can be prescribed along with a desired compression time; for the simulation results presented here CR_{max} has been set to 13.4 and Δt_{comp} fixed at 15.3 ms. It should be noted that for all of the cases studied here the evaporation process is completed before the maximum compression ratio, or overall compression time is reached. These parameters are important however because they affect the trajectory of the compression process, and thus volume history which regulates the droplet vaporization. The volume trace employed for this study is illustrated in Fig. 2 along with representative curves for the temperature and pressure as well as the instantaneous compression ratio. For this example an initial temperature and pressure of T_0 = 350 K and P_0 = 0.44 bar, respectively, are used with a pre-vaporized mixture of *n*-dodecane and air at an overall equivalence ratio of φ = 1.0. Under conditions of no chemical reaction a compressed temperature and pressure near T_{comp} = 790 K and P_{comp} = 13.3 bar, respectively, results for this case. For a chemically reacting case, ignition is predicted using the detailed kinetic mechanism of Westbrook et al. [27] (2115 species, 8157 reactions). Here it can be seen that significant low temperature heat release (LTHR) occurs just before maximum compression is reached, with the second-stage heat release occurring shortly after this. It is apparent that during aerosol RCM tests using similarly reactive fuels where the charge is prepared *in situ*, fuel vaporization and diffusive mixing must be completed well in advance of conditions where chemical reactivity becomes sufficiently rapid. Evident in Fig. 2 is that the pressure rise during compression is most significant during the later stage of the compression process; the rise in temperature follows a similar non-linear trend, however this curvature is not as steep. These features significantly affect the evaporation process for some fuels and operating conditions where substantial volumetric compression is required to achieve complete fuel evaporation (e.g., φ = 2.0). For such conditions there is a large corresponding reduction in the reaction chamber volume which can lead to high ratios of surface area to volume and thus high levels of heat loss from the test gases. In addition, flows of the aerosol into the piston's machined crevice regions or ringpack can become significant at high *CR* and this can alter the thermodynamic state of the compressed charge, as well as contaminate the surfaces of, or gap into the crevice volume. The non-linearity of the temperature rise can also affect gas-phase stratification during aerosol operation, as the time available for heat and mass transport to and from the droplet, respectively, becomes shorter for successive increments in compression heating. These issues will be discussed shortly.

The following results illustrate the influence of initial droplet size and overall fuel loading on the evaporation characteristics of the fuel aerosols. The fuel loadings are specified according to Table 1 where the ratios of initial 'far-field' radius to the droplet radius are listed. These are prescribed for the conditions of T_0 = 350 K and P_0 = 1.0 bar, and an initial liquid-phase density of ρ_l = 0.734 g/cm^3. The initial temperature was selected because it is within the range of a heated RCM (e.g., $T_{limit} \sim 375$ K due to seal degradation issues). The initial pressure of 1.0 bar yields a compressed pressure near 28 bar which is useful for acquiring data relevant to combustion engine operating regimes.

3.1. Initial droplet size

Figures 3–6 present results for a series of runs where the initial droplet diameter is varied from d_0 = 2 to 14 μm. The smallest droplet has a Knudsen number of $Kn_0 \sim 0.03$, while the largest has $Kn_0 \sim 0.004$, based on droplet radius. This is within the lower bounds of the Knudsen transition region ($0.01 < Kn < 10$). Based on the results of Sazhin et al. [21] and a non-equilibrium evaporation model (see Appendix A) however, it is expected that only modest errors (~5–15%) will result due to the use of the interface equilibria model. Two equivalence ratios are shown in these figures including φ = 0.0 and 1.0; the φ = 0.0 condition represents an isolated droplet case for comparison.

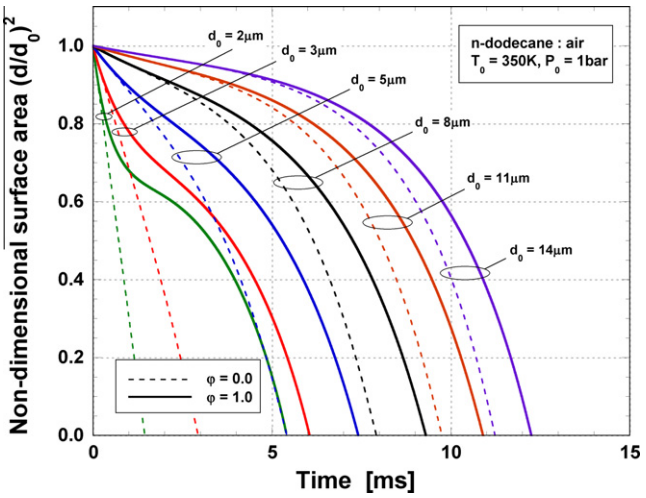

Fig. 3. Non-dimensional droplet surface areas as a function of time for various sized droplets of *n*-dodecane in air at an initial temperature and pressure of $T_0 = 350$ K and $P_0 = 1$ bar, respectively, at two fuel loadings.

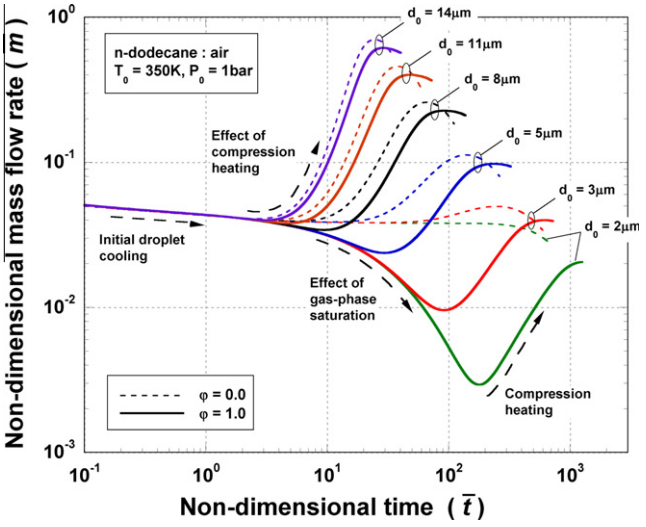

Fig. 4. Non-dimensional evaporation rates as a function of non-dimensional time for various sized droplets of *n*-dodecane in air using an initial temperature and pressure of $T_0 = 350$ K and $P_0 = 1$ bar, respectively, at two fuel loadings.

In Fig. 3 the non-dimensional surface area, $(d/d_0)^2$, is plotted as a function of time. For the smallest droplet at the $\varphi = 0.0$ condition it can be seen that there is almost no effect of the volumetric compression process on the evaporation of the droplet. Typical d^2-law behavior is seen with a slight positive concavity due to the initial droplet cooling that results from the initialization conditions considered in this study [16]. The mostly, linear behavior results because the evaporation process is fast enough so that the droplet is consumed before the piston-driven reaction chamber volume is noticeably changed. For the larger (isolated) droplets however there is a substantial departure from linear d^2-law behavior due to the compression heating process; this feature is discussed in detail in Ref. [16]. The evaporation times for these cases are substantially shortened due to the significant increase in droplet temperature and corresponding saturation pressure caused by compression. It should be stressed here that these evaporation simulations are different from typical droplet studies where cool droplets are introduced into elevated temperature environments, such as in a diesel engine or continuous flow vaporization rig

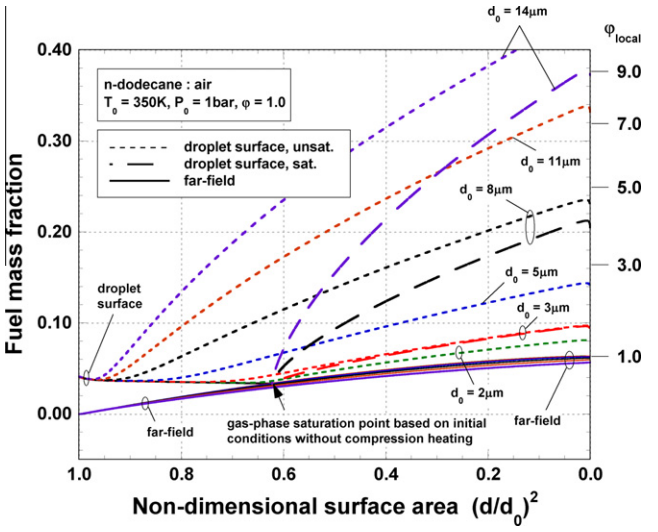

Fig. 5. Gas-phase fuel mass fractions at the droplet surface and at the 'far-field' as a function of non-dimensional surface area for a range of initial droplet sizes at an overall stoichiometric ratio ($\varphi = 1.0$). Simulation results using initially saturated gas-phase conditions are also presented for three droplet sizes, $d_0 = 3$, 8 and 14 μm.

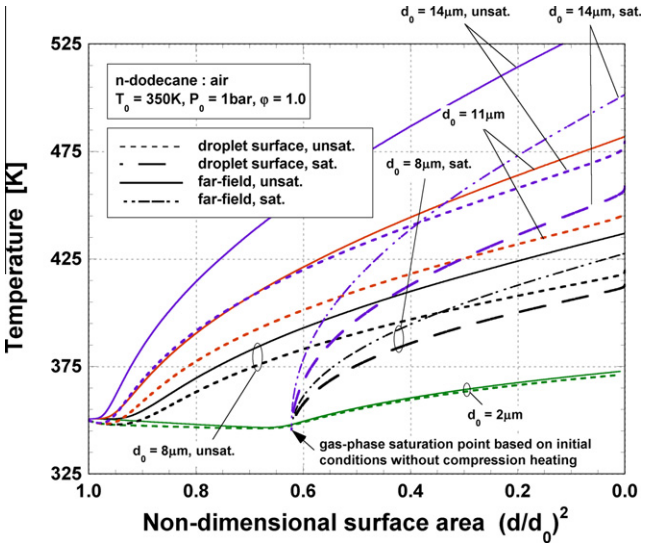

Fig. 6. Gas-phase temperatures at the droplet surface and at the 'far-field' as a function of non-dimensional surface area for a range of initial droplet sizes at an overall stoichiometric ratio ($\varphi = 1.0$). Simulation results using initially saturated gas-phase conditions are also presented for two droplet sizes, $d_0 = 8$ and 14 μm.

[28], where the droplets undergo initial heating and sometimes volumetric expansion to their respective boiling points. For the stoichiometric cases, all of the evaporation times are longer relative to the $\varphi = 0.0$ condition. This is due to the effects of droplet–droplet interactions where gas-phase fuel saturation and evaporative cooling results. The smallest droplet is most noticeably affected with the evaporation time increased by +350%; the largest droplet experiences an increase in evaporation time by only +9%. Thus the fuel saturation and evaporative cooling effects render the evaporation process less size dependent. To better understand this behavior Figs. 4–6 are presented.

In Fig. 4 the non-dimensional mass flow rates, defined as $\bar{m} = \dot{m}/4\pi\rho_g D_g r_s$, are plotted as a function of non-dimensional time, defined as $\bar{t} = \int \kappa_l dt / r_s^2$, for all of the cases shown in Fig. 3. Here $\dot{m}$ is the mass flow rate from the droplet (i.e., the evaporation rate), ρ_g the gas-phase density, D_g the mass diffusion coefficient in

the gas-phase, r_s the instantaneous radius of the droplet surface, $\hat{\kappa}_l$ the average liquid-phase thermal diffusivity and t the time. Changes in ρ_g, D_g and $\hat{\kappa}_l$ with time (i.e., T, P) are included in the calculation of $\dot{m}$ where these effects are most noticeable at long times and for the largest droplets; the trends though, are found to be the same if constant property values are used. In Fig. 4 the effect of initial droplet cooling is highlighted where the vaporization rates are slightly reduced during the initial portion of the process. For the $\varphi = 0.0$ condition the trajectory of the $d_0 = 2$ μm droplet is fairly constant throughout its lifetime again illustrating that there is no effect of gas-phase compression on its evaporation process. The larger droplets however experience increasing rates of evaporation as the near-droplet temperature and corresponding saturation pressure are increased. For the $\varphi = 1.0$ condition saturation effects are noticeable. At this fuel loading the trajectories of the smaller droplets (e.g., $d_0 < 8$ μm) depart significantly from the isolated droplet cases because gas-phase saturation causes the rates of evaporation to decrease. This effect is most severe for the $d_0 = 2$ μm droplet because the 'far-field' boundary is much closer to the droplet surface and therefore the fuel can diffuse to it more quickly. As the volumetric compression process begins the rates of evaporation are then increased and this causes the droplets to vaporize more quickly.

Figure 5 illustrates the issue of 'far-field' fuel saturation for the $\varphi = 1.0$ condition. In this figure the fuel mass fractions at the droplet surface and at the 'far-field' are plotted as a function of non-dimensional surface area for the six droplet sizes shown in Fig. 3. First, it can be seen in this figure that the trajectories of the 'far-field' concentrations are very similar for all of the cases with the final concentration near $Y_{\text{fuel}} \sim 0.062$. This is the overall mass fraction of fuel specified by the $\varphi = 1.0$ condition. This result indicates that for all of the cases there is a fair degree of fuel distribution within the gas-phase by the time the evaporation process is complete. The behavior of the fuel concentration at the droplet surface however is quite different for the six droplet sizes shown here. This feature is due to the effects of gas-phase volumetric compression heating where, for example, the smallest droplet experiences evaporation and gas-phase transport that are rapid enough so that the gas-phase almost completely saturates by the time the compression heating process begins. Conversely, for the largest droplet ($d_0 = 14$ μm) there is not much fuel evaporation, and therefore surface area reduction, before the compression process begins to significantly heat the droplet and correspondingly increase its saturation pressure. The compression heating results in higher levels of Y_{fuel} at the droplet surface. The largest droplet experiences the greatest increase in temperature throughout its lifetime, and therefore the fuel mass fraction at the droplet surface is the highest for this case. From these trajectories it can be inferred that there is a substantial level of fuel stratification near the droplet surface by the end of the evaporation process.

To investigate the effect of the initialization scheme used for these simulations (i.e., no fuel in the gas-phase, volumetric compression beginning near $t = 1$ ms, etc.) on the extent of fuel stratification, three additional cases are simulated with $d_0 = 3$, 8 and 14 μm where the gas-phase is instead assumed to be initially saturated with fuel. The initial temperature and pressure for these runs are $T_0 = 345.5$ K and $P_0 = 0.988$ bar, respectively; these are the conditions that result if the fuel droplets are allowed to sit for a long period of time before the gas-phase is compressed. This may be a more realistic starting condition for droplets in an aerosol that is generated upstream of the RCM where there is sufficient residence time within the delivery manifold so that some pre-compression evaporation occurs. The fuel concentration at this condition is $Y_{\text{fuel}} = 0.033$. The initial droplet diameters are adjusted so that the overall equivalence ratio is 1.0; based on the values listed above this is when $(d/d_0)^2 = 0.622$. The same piston position versus time trajectory is used to specify the volumetric compression profile.

The results for these three cases are also presented in Fig. 5 where the fuel mass fraction at the droplet surface is plotted; these are labeled as 'droplet surface, sat.' in the figure legend. The fuel concentrations at the 'far-field' are indistinguishable from the other runs and therefore these are not included. The results of these additional simulations indicate that while the overall evaporation times are reduced relative to the previous initialization scheme, there is only a small effect on the extent of near-droplet fuel stratification that ensues. Large droplets are still predicted to result in substantial levels of fuel stratification at the droplet surface. This issue could be problematic during RCM experiments because the reaction progress may be altered by locally high concentrations; the fuel would need to diffusively mix across the gas-phase by the time chemical reactions become significant. At temperatures near 600–750 K, which is in the NTC (negative temperature coefficient) region, ignition times can be reduced by factors of two to ten for fuel-rich mixtures (e.g., $\varphi > 2.0$) relative to stoichiometric ones [29]. Localized fuel stratification could considerably complicate interpretation of aerosol RCM ignition data. Though it is not indicated here, the stratification shown in Fig. 5 requires approximately 100–300 μs after the end of evaporation to completely dissipate.

Figure 6 next presents an indication of the thermal stratification that develops during the wet compression process; this is for the droplet sizes shown in Fig. 5; for clarity the results for the $d_0 = 3$ and 5 μm cases are not included here. The temperatures at the droplet surface and at the 'far-field' are plotted as a function of non-dimensional surface area; the $d_0 = 8$ and 14 μm cases using the saturated initial conditions are also shown here. As with fuel concentration, it can be seen that the thermal stratification is more significant for the largest droplets; there is also significant stratification that develops for the saturated initial cases. An interesting feature when comparing Figs. 5 and 6 is that the compositional stratification is much more substantial than the thermal stratification. This is due to the high Lewis numbers of these mixtures ($Le_g = \kappa_g/D_g \sim 3.8$) where thermal diffusion is more rapid than mass diffusion. Similarly high Lewis numbers exist for fuel–air mixtures of other large hydrocarbon and transportation-relevant fuels. In Ref. [26], comparisons are made with water droplets where the Lewis number is significantly different, e.g., $Le_g \sim 0.9$; in those cases thermal stratification is more significant than compositional stratification.

3.2. Fuel loading

Figures 7–9 present results for a series of runs where the fuel loadings are varied from $\varphi = 0.0$ to 2.0; this range is typical for RCM experiments [12,25]. In Fig. 7 the non-dimensional surface areas are plotted as a function of time for four fuel loadings where an initial diameter of $d_0 = 3$ μm is used. The effect of increasing gas-phase saturation on the evaporation rate becomes increasingly visible for the higher levels of fuel loading; greater extents of compression heating are required in order to completely evaporate the droplets. This should be expected as the overall vaporization enthalpy increases for higher fuel loadings.

Figure 8 illustrates the fuel mass fraction at the droplet surface and at the 'far-field' for these four cases. Similar behavior is seen as with Fig. 5. For the lowest fuel loading case (i.e., the isolated droplet), there is almost no change in the surface fuel concentration throughout the lifetime of the droplet; this is due primarily to the short evaporation time as well as the lack of 'far-field' saturation. However, for the highest fuel loading case (i.e., $\varphi = 2.0$) the 'far-field' quickly saturates, and significant compression heating is required in order to vaporize all of the fuel. It is interesting to

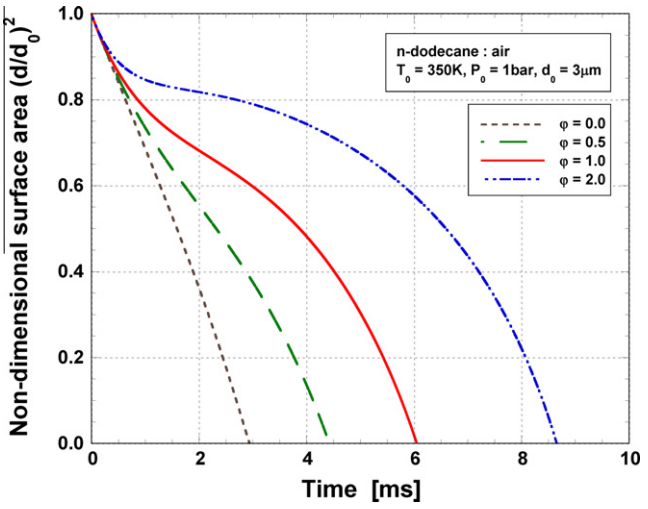

Fig. 7. Non-dimensional droplet surface areas as a function of time for $d_0 = 3$ μm droplets in air at initial temperature and pressure of $T_0 = 350$ K and $P_0 = 1$ bar, respectively, at various fuel loadings.

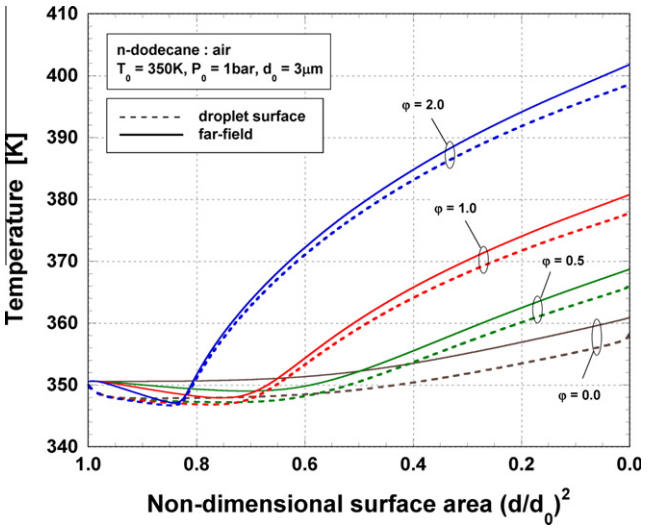

Fig. 9. Gas-phase temperatures at the droplet surface and at the 'far-field' as a function of non-dimensional surface area for $d_0 = 3$ μm droplets at various fuel loadings.

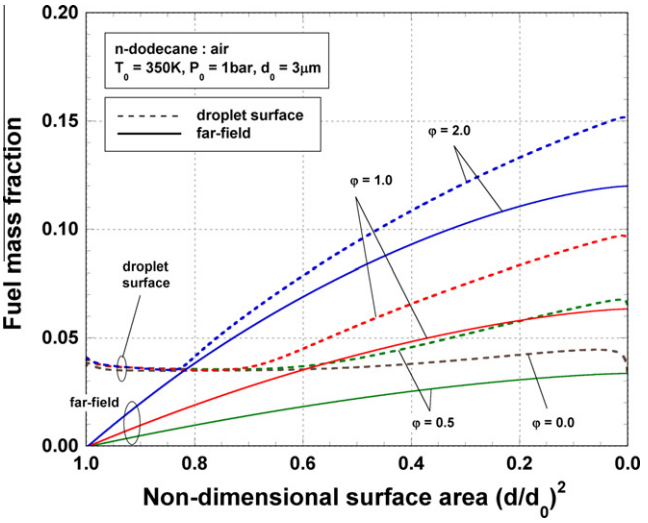

Fig. 8. Gas-phase fuel mass fractions at the droplet surface and at the 'far-field' presented as a function of non-dimensional surface area for $d_0 = 3$ μm droplets at various fuel loadings.

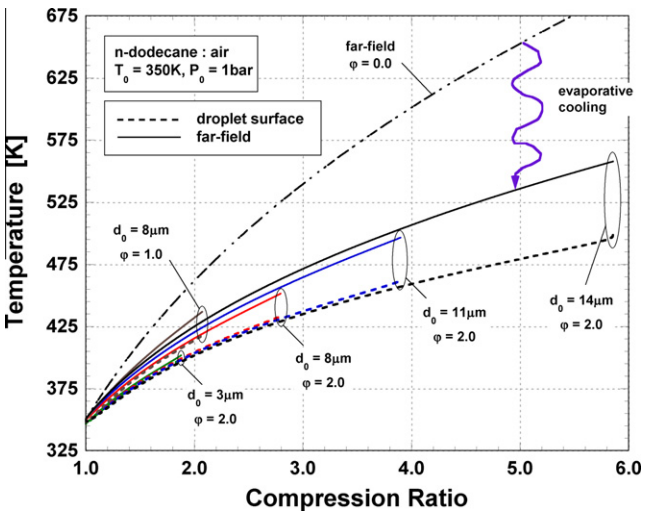

Fig. 10. Gas-phase temperatures at the droplet surface and at the 'far-field' as a function of compression ratio for various droplet sizes and at various fuel loadings.

note that the extent of fuel stratification (i.e., $\varphi_s - \varphi_\infty$) for the three fuel loadings ($\varphi = 0.5$, 1.0 and 2.0) is very similar.

Figure 9 next illustrates the temperatures at the droplet surface and at the 'far-field' for the four cases from Fig. 8. Here it can be seen that there is a slight increase in the temperature of the 'far-field' for the isolated droplet case, while a larger temperature rise (~50 K) is experienced for the highest fuel loading; this indicates the extent of compression heating required to overcome the saturation limit of the fuel. As with Figs. 5 and 6, it can be seen when comparing Figs. 8 and 9 that the compositional stratification is more substantial than the thermal stratification for all of the fuel loadings, with this again due to the high *Le* for these mixtures.

Figure 10 next illustrates the level of evaporative cooling that results from fuel evaporation during wet compression. The droplet surface and 'far-field' temperatures are plotted as a function of instantaneous compression ratio for three fuel loadings, $\varphi = 2.0$, 1.0, and 0, respectively. The complete consumption points for each of the droplets are indicated. Again noticeable in this figure is the temperature difference between the droplet surface and the 'far-field'; the larger droplets experience greater temperature increases and greater levels of stratification. In addition, the extent of evaporative cooling is highlighted for the $d_0 = 14$ μm, $\varphi = 2.0$ case where the 'far-field' experiences a drop in temperature of nearly 20%, while the $\varphi = 1.0$ case results in a temperature drop at the 'far-field' of only ~7%. Also observable in this figure is that because the larger droplets and higher fuel loadings experience greater extents of compression heating, the corresponding compression ratio and thus volume change of the reaction chamber is greater. This feature can lead to a number of difficulties concerning practical implementation of wet compression in an aerosol RCM, especially at high φ. These include: (i) ensuring that the localized stratification is minimized/eliminated before the RCM test conditions are reached (which could be difficult at high *CR* where relative times to reach the test conditions (e.g., CR_{max}) are shorter, (ii) ensuring that the fuel droplets within the aerosol have limited interaction with the walls of the chamber during the long stroke of the RCM's piston, and (iii) preventing significant flow of the fuel droplets into the piston's machined crevice volume at high *CR*.

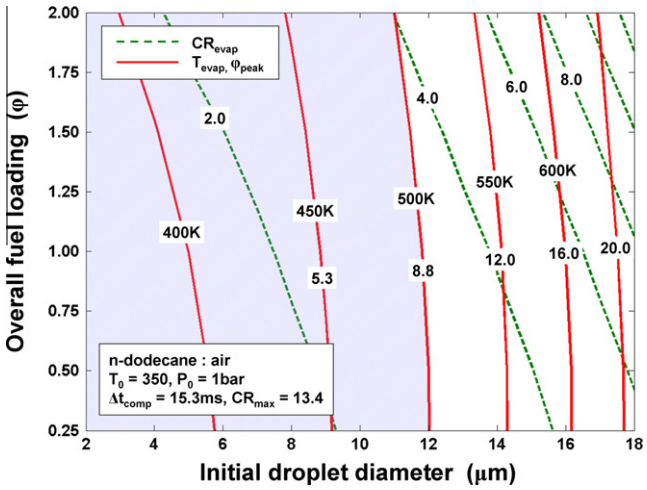

Fig. 11. Predicted 'operating map' for an aerosol RCM fueled with *n*-dodecane + air where the compression ratio, peak gas-phase temperature and peak equivalence ratio at the end of the vaporization process are indicated for a range of initial droplet diameters at various fuel loadings. The shaded region will yield complete fuel evaporation before the low temperature chemistry limit (~500 K) is reached.

An 'operating map' is last presented in Fig. 11 to summarize the findings of this study where the extents of compression heating required and levels of fuel stratification that develop in the gas-phase are indicated for a range of initial droplet sizes at various fuel loadings; the initial temperature and pressure are set to $T_0 = 350$ K and $P_0 = 1$ bar for this figure. Iso-pleths are drawn for the compression ratio, peak gas-phase temperature and peak fuel equivalence ratio at the end of the evaporation process; as seen in Figs. 5 and 6, the peak gas-phase temperature occurs at the 'far-field' boundary while the peak equivalence ratio is at the droplet surface. In this figure it is observed that the highest volumetric compression is required for the largest droplets at the highest fuel loadings, as should be expected. Also observed is that T_{evap} and φ_{evap} are fairly constant for a particular droplet size over a range of fuel loadings. This is due primarily to the increasing level of evaporative cooling that occurs with higher fuel loadings, as indicated in Fig. 10. Also shown in Fig. 11 is the range of conditions (the shaded region) where the wet compression process is predicted to complete before $T_{evap} \sim 500$ K; this again, is considered as a low temperature chemistry limit. The localized gas-phase fuel stratification that develops during the wet compression process should be expected to quickly dissipate so that locally homogenous chemical reactions will occur during the RCM test.

4. Summary

A spherically-symmetric, diffusion-limited, transient wet compression model has been used to investigate the evaporation behavior of fuel aerosols subjected to rapid gas-phase compression (i.e., wet compression). Droplet–droplet interaction under rapid compression machine (RCM) conditions can result in significant gas-phase fuel saturation and evaporative cooling, especially under high concentration aerosols (e.g., ~0.1 mL_{fuel}/L_{gas} (~1×10^9 drops/L_{gas}) for stoichiometric fuel loading at ambient conditions). These effects are studied where the initial droplet size and overall fuel loading are varied. *n*-Dodecane is used as the fuel with the gas containing air (21% O_2 and 79% N_2). An overall compression time and compression ratio of 15.3 ms and 13.4, respectively, are used. Through this study we have found that smaller droplets ($d_0 \sim 2$–3 μm) are more affected by 'far-field' saturation and evaporative cooling effects, while larger initial droplets ($d_0 \sim 14$ μm) result in a greater degree of compositional and thermal stratification in the gas-phase due to longer diffusion distances. Consequently, for larger droplets, the interpretation of the resulting ignition data may be problematic. Larger droplets are also more affected by the volumetric compression process under RCM conditions since they require more time for vaporization to complete. All of the cases explored here yield a greater degree of fuel stratification than thermal stratification due to the high Lewis numbers for the fuel–air mixtures ($Le_g \sim 3.8$).

Based on the results of this study it appears that the aerosol RCM concept is feasible for investigating the low temperature ignition behavior of transportation-relevant, involtile fuels. However, aerosol generation systems which can deliver high concentrations of very small droplets (e.g., $d_0 < 3$–5 μm, ~0.1 mL_{fuel}/L_{gas}) should be utilized in order to minimize localized (i.e., on the droplet scale) stratification issues and achieve vaporization at lower compression ratios. Systems which can tailor the machine's compression time and compression ratio, as well as the diluent gas composition for a range of fuels could prove versatile for such investigations. A companion study [26] investigates the effects of fuel boiling and transport characteristics as well as diluent gas thermo-physical properties to support future machine design efforts.

Acknowledgments

Professor Rolf Reitz at the University of Wisconsin Engine Research Center is thanked for his assistance in locating a copy of the original source code for the transient droplet evaporation model. Funding for this work has been provided in part through NSF CBET-0521602. The simulations were conducted using the Cluster Computing Center at Marquette University.

Appendix A

The wet compression model employed in this study is summarized here. The model integrates a transient droplet evaporation sub-model with a gas-phase volumetric compression step. The evaporation sub-model is based on the work of Aggarwal and co-workers [17–19] and utilizes a continuum formulation for a spherically-symmetric droplet taking into account thermal and concentration gradients within the droplet, variations in liquid- and gas-phase properties with temperature and pressure, and real gas behavior. The model is modified for this study in order to utilize no-flux (i.e., no-gradient) boundary conditions at the 'far-field' and to incorporate a thermodynamic non-equilibrium condition at the droplet surface. The no-flux boundary enables various levels of fuel loading (i.e., equivalence ratio, φ) to be simulated by adjusting the initial size of the computational mesh, i.e., the location of the 'far-field' boundary. The non-equilibrium condition enables an assessment of the importance of gas kinetic effects near the droplet surface. For the droplets investigated in this work gas kinetic effects are found to be modest (i.e., +5–10% error in total evaporation times).

The transient two-phase governing equations are written in spherical coordinates with appropriate interface conditions prescribed at the droplet surface. Radiation and second-order effects, such as Soret and Dufour effects, are assumed to be negligible. The model considers mass, species, momentum and energy conservation throughout the gas-phase domain and it considers absorption of gas into the liquid-phase, while resolving species diffusion processes within the droplet. Within the computational framework, both the gas- and liquid-phase properties are considered to be functions of species, temperature and pressure, and an adaptive grid is used to account for the surface regression. An operator splitting technique is incorporated to physically compress the

computational mesh at each time step to account for compression heating of the gas-phase. The governing equations and the interphase conditions at the droplet surface are reviewed next.

A.1. Governing equations

For the gas-phase region $r > r_s(t)$, the governing equations include the conservation equations for mass, species, momentum, energy and the equation of state (EOS):

$$\frac{\partial \rho_g}{\partial t} + \frac{1}{r^2}\frac{\partial}{\partial r}\left(\rho_g u r^2\right) = 0 \tag{A1}$$

$$\frac{\partial \rho_{gk}}{\partial t} + \frac{1}{r^2}\frac{\partial}{\partial r}(\rho_{gk} u r^2) = \frac{1}{r^2}\frac{\partial}{\partial r}\left[\rho_g D_{gk} r^2 \frac{\partial Y_k}{\partial r}\right] \tag{A2}$$

$$\frac{\partial \rho_g u}{\partial t} + \frac{1}{r^2}\frac{\partial}{\partial r}(\rho_g u^2 r^2) + \frac{\partial P}{\partial r} = \frac{1}{r^2}\frac{\partial}{\partial r}\left[2\mu_g r^2 \frac{\partial u}{\partial r} + \lambda_g \frac{\partial}{\partial r}(ur^2)\right] - \frac{2}{r^2}\left[2\mu_g u + \frac{\lambda_g}{r}\frac{\partial}{\partial r}(ur^2)\right] \tag{A3}$$

$$\frac{\partial \rho_g}{\partial t} + \frac{1}{r^2}\frac{\partial}{\partial r}(\rho_g I u r^2) + \frac{P}{r^2}\frac{\partial}{\partial r}(ur^2) = \frac{1}{r^2}\left\{\frac{\partial}{\partial r} r^2 \rho_g \left[\sum_{k=1}^{N} D_{gk} h_{gk} \frac{\partial Y_k}{\partial r}\right]\right\} + \frac{1}{r^2}\frac{\partial}{\partial r}\left(\alpha_g r^2 \frac{\partial T_g}{\partial r}\right) + \frac{\partial u}{\partial r}\left[2\mu_g \frac{\partial u}{\partial r} + \frac{\lambda_g}{r^2}\frac{\partial}{\partial r}(ur^2)\right] + \frac{2u}{r^2}\left[2\mu_g u + \frac{\lambda_g}{r}\frac{\partial}{\partial r}(ur^2)\right] \tag{A4}$$

$$f_1(T_g, P, \rho_{g1}, \rho_{g2}, \ldots, \rho_{gN}) = 0 \tag{A5}$$

In Eqs. (A1)–(A5), t and r refer to temporal and spatial variables, respectively, and ρ_{gk}, D_{gk}, Y_k, and h_{gk} represent the gas-phase density, diffusion coefficient, mass fraction and specific enthalpy of the kth species, respectively, with N the total number of species. The parameters α_g, μ_g, and λ_g are the gas-phase thermal conductivity, viscosity, and second viscosity coefficient, respectively. In addition, u is radial velocity, T_g temperature, P pressure and I mass-specific internal energy. Eq. (A5) is a P–ρ–T relation for the fluid mixture, such as the ideal gas or Peng-Robinson EOS. For the conditions explored in this study the PR-EOR is utilized, though the ideal gas EOS could be used with negligible error.

For the liquid-phase region, $r < r_s(t)$, the governing equations include only species and energy diffusion

$$\frac{\partial \rho_{lk}}{\partial t} = \frac{1}{r^2}\frac{\partial}{\partial r}\left[\rho_{lk} D_{lk} r^2 \frac{\partial X_k}{\partial r}\right] \tag{A6}$$

$$\frac{\partial}{\partial t}(\rho_l c_{pl} T_l) = \frac{1}{r^2}\frac{\partial}{\partial r}\left(\alpha_l r^2 \frac{\partial T_l}{\partial r}\right) + \frac{1}{r^2}\left\{\frac{\partial}{\partial r} r^2 \left[\sum_{k=1}^{N} \rho_l D_{lk} h_{lk} \frac{\partial X_k}{\partial r}\right]\right\} \tag{A7}$$

In these expressions the subscript 'l' denotes the liquid-phase, and c_p is the specific heat at constant pressure; X_k is the mass fraction of species k in the liquid-phase.

A.2. Boundary conditions

The boundary conditions at the droplet center ($r = 0$) are: $\partial T_l/\partial r = 0$ and $\partial \rho_k/\partial r = 0$; for the 'far-field' (i.e., $r = r_\infty$) no-gradient and no-velocity boundary conditions are applied to ensure that mass, momentum, energy and species cannot enter or leave the computational domain, i.e., the reaction chamber volume: $\partial \rho_{k,\infty}/\partial r = 0$, $\partial \rho_\infty/\partial r = 0$, $u_\infty = 0$, and $\partial T_\infty/\partial r = 0$. At the liquid–vapor interface, $r = r_s(t)$, two different approaches are used, including thermodynamic equilibrium and thermodynamic non-equilibrium.

A.2.1. Liquid–vapor equilibrium at the droplet surface

Under thermo-mechanical equilibrium conditions mass and energy conservation can be expressed as

$$m'' X_k - \rho_{lk} D_{lk} \left.\frac{\partial X_k}{\partial r}\right|_{r=r_s^-} = m'' Y_k - \rho_{gk} D_{gk} \left.\frac{\partial Y_k}{\partial r}\right|_{r=r_s^+} \tag{A8}$$

$$-\alpha_l \left.\frac{\partial T_l}{\partial r}\right|_{r=r_s^-} = -\alpha_g \left.\frac{\partial T_g}{\partial r}\right|_{r=r_s^+} + \sum_{k=1}^{N}\left(m'' Y_k - \rho_{gk} D_{gk}\frac{\partial Y_k}{\partial r}\right)\Big|_{r=r_s^+} L_k + m''\left[\frac{u^2}{2} - u\frac{dr_s}{dt} - \frac{2\mu_g}{\rho}\frac{\partial u}{\partial r} + \frac{\lambda_g}{r^2}\frac{\partial}{\partial r}(ur^2)\right] \tag{A9}$$

where m'' is the net vaporization flux from the droplet, and X_{ks} and Y_{ks} represent, respectively, the liquid- and gas-phase mole fractions of these species at the droplet surface. The latent heat of vaporization of species k is L_k. In addition, the temperature, pressure and fugacity of each species in the gas-phase is specified to be equal to the corresponding property of the same species in the liquid-phase. The equality of the fugacity of species k is expressed as

$$\phi_k^g Y_k = \phi_k^l X_k \tag{A10}$$

where φ_k is the fugacity coefficient of the kth species, which is a function of pressure, temperature and composition. It is given in terms of the volumetric properties of the mixture by the following thermodynamic relation

$$RT\ln(\phi_k) = \int_{\upsilon}^{\infty}\left[\left(\frac{\partial P}{\partial n_k}\right)_{T,\upsilon,n_j} - \frac{RT}{\upsilon}\right]d\upsilon - RT\ln z \tag{A11}$$

where n_j is the mole number of the jth species and z is the compressibility factor, $z = PU/RT$. R is the gas constant and U the specific volume of the mixture.

A.2.2. Thermodynamic non-equilibrium at the droplet surface

To investigate effects of non-equilibrium at the droplet surface, which are important for small droplet sizes where the Knudsen number ($Kn = \eta/r_s$) is close to unity, the equilibrium expressions are modified as follows. A two-zone model is implemented at the surface of the droplet where an inner zone accounts for free-molecular flow while the outer zone considers continuum behavior. A schematic of this is illustrated in Fig. A1. In the free-molecular region the rate of collisions of gas particles with the droplet surface is the rate-limiting factor. In this region it is assumed that most of the particles do not collide with other particles before they collide with the droplet, or move into the continuum zone. The free-molecular zone is assumed to meet the continuum zone at a distance ζ from the droplet surface where ζ is considered to be on the order of the mean free path of the

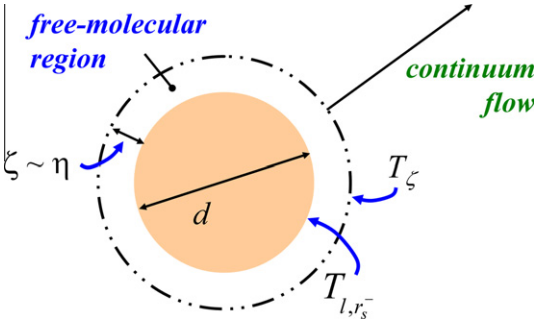

Fig. A1. Schematic of the two-zone non-equilibrium model illustrating the continuum and free-molecular regions. The scale of ζ is exaggerated in this figure; it is on the order of ~5–15% of the droplet diameter during most of the droplets' lifetime.

molecules, η. At the zonal interface the rates of mass and heat transport are set equal to the transport rates at the droplet surface.

Using this model the fugacity coefficient from Eq. (A10), applied at the zonal interface can be adjusted such that

$$\phi_k^l = \phi_k^{l^*} - \frac{\Delta P_k}{P} \tag{A12}$$

where φ_k^{l*} represents the liquid-phase fugacity coefficient of the kth species under phase equilibrium conditions (i.e., as determined from Eq. (A11)). The second term of this expression is sometimes referred to as the Hertz-Knudsen correction and can be expressed as

$$\frac{\Delta P_k}{P} = \frac{\sqrt{2\pi RT/MW_k}}{P\delta_k^m} m_k'' \tag{A13}$$

Here δ_k^m is the mass accommodation, or evaporation coefficient of the kth species where this has a range from 0.0 to 1.0. P is the total pressure at the liquid–vapor interface.

The energy transport at the droplet surface is reformulated as

$$-\alpha_l \frac{\partial T_l}{\partial r}\bigg|_{r=r_s^-} = \sum_{k=1}^{N}(1-\delta_k^m)\delta^T \frac{\rho_{gk}}{MW_k}\sqrt{\frac{RT_{l,r_s^-}}{2\pi MW_k}}\left(c_{v,k}+\frac{R}{2}\right)(T_{l,r_s^-}-T_\zeta) + \sum_{k=1}^{N} m'' Y_k\bigg|_{r=r_s^+} L_k \tag{A14}$$

where the first term on the right hand side is the energy transferred to the liquid-phase due to gas-phase particles that strike the droplet and rebound. In this expression T_ζ is the temperature at the interface between the free-molecular and continuum zones while T_{l,r_s^-} represents the surface temperature of the droplet. The thermal accommodation coefficient, δ^T, is defined as

$$\delta^T = \frac{T_\zeta - T'}{T_\zeta - T_{l,r_s^-}} \tag{A15}$$

with T' representing the temperature of the particles after they rebound from the droplet surface. In Eq. (A14) $c_{v,k}$ is the specific heat at constant volume of the kth species in the gas-phase while Y_k is the *corrected*, non-equilibrium gas-phase mass fraction of the kth species.

The energy transport at the zonal interface can then be equated to the transport at the droplet surface,

$$\begin{aligned}&\sum_{k=1}^{N}(1-\delta_k^m)\delta^T \frac{\rho_{gk}}{MW_k}\sqrt{\frac{RT_{l,r_s^-}}{2\pi MW_k}}\left(c_{v,k}+\frac{R}{2}\right)(T_{l,r_s^-}-T_\zeta) + \sum_{k=1}^{N} m'' Y_k\bigg|_{r=r_s^+} L_k \\ &= -\alpha_g \frac{\partial T_g}{\partial r}\bigg|_{r=r_s^+ +\zeta} + \sum_{k=1}^{N}\left(m'' Y_k - \rho_{gk} D_{gk}\frac{\partial Y_k}{\partial r}\right)\bigg|_{r=r_s^+ +\zeta} L_k \\ &\quad + m''\left[\frac{u^2}{2} - u\frac{dr_s}{dt} - \frac{2\mu_g}{\rho}\frac{\partial u}{\partial r} + \frac{\lambda_g}{r^2}\frac{\partial}{\partial r}(ur^2)\right]\end{aligned} \tag{A16}$$

These expressions along with Eqs. (A8)–(A11), provide a closed system to determine the temperature and species mole fractions at the droplet surface. It represents a system of tightly coupled, nonlinear algebraic equations that are solved iteratively at each time step.

An improved modeling approach for thermodynamic non-equilibrium behavior has recently been developed by Sazhin and coworkers [21,23] where the kinetic zone prescribed around the droplet is extended to 10 times η, and the dynamics of the molecules within this inner zone, including both fuel vapor and oxidizer + diluent, are described in terms of the more rigorous Boltzmann equations. Both heat and mass fluxes across this zone are taken into account, as is done here. Their approach is more accurate and should probably be used for design-relevant calculations, especially if extremely small droplets will be utilized (e.g., $d_0 \sim 1$ μm). For the current study however, the simpler model described above is thought to be adequate for assessing the impacts of thermodynamic non-equilibrium on the wet compression simulation results.

To account for multiple components in the liquid-phase (e.g., fuel + oxidizer or diluent gas) the latent heat of vaporization of each species is defined as the difference between the partial molar enthalpy of that species in the vapor and liquid-phases. The following expression then gives the partial molar enthalpy of the kth species:

$$L_k = h_{lk} - h_k^0 = -RT^2\frac{\partial}{\partial T} ln\,\phi_k \tag{A17}$$

where the superscript '0' denotes the property in the ideal gas state.

A.3. Gas-phase compression heating

The gas-phase compression process is computed by physically compressing the mesh at each time step thereby increasing the density of the computational cells and the associated internal energy. This process is assumed to occur adiabatically so that the new cell specific internal energy can be determined based on energy conservation

$$I_{ii}^{n+1} = I_{ii}^n - \int_{v_{ii}^n}^{v_{ii}^{n+1}} P_{ii}\,dv \tag{A18}$$

with ii indicating the iith computational cell. The PR-EOS is used in conjunction with this expression to iteratively determine the resulting cell pressure and temperature. Momentum of each gas-phase cell is also conserved during the compression operation, where this is expressed as

$$(\rho_g u^2 r^2)_{ii}^{n+1} = (\rho_g u^2 r^2)_{ii}^n \tag{A19}$$

A.4. Solution procedure

An arbitrary Lagrangian–Eulerian numerical method with a dynamically adaptive mesh is used to solve the governing equations. The solution procedure is as follows: (i) calculate explicitly the contributions of the diffusion and source terms in the gas-phase equations, (ii) calculate implicitly the terms associated with the acoustic pressure in the gas-phase equations; (iii) compute a new mesh distribution due to droplet surface regression using the adaptive mesh method, and then the convective terms in the gas-phase equations, (iv) based on the solutions of the above steps, solve implicitly the gas-phase equations, along with the liquid-phase equations and the droplet surface and liquid–vapor interface equations, and (v) perform the gas-phase compression step.

An algorithm is employed in this study to adaptively resize the gas-phase computational cells based on the magnitude of temperature gradients across the domain; higher grid densities are used near the droplet surface where higher gradients exist. A variable time step is also utilized where this is automatically adjusted depending on stability criteria of the explicit convection and diffusion processes.

A.5. Thermo-physical models

The gas- and liquid-phase thermo-physical properties are considered to be functions of pressure, temperature and composition where the activity coefficient is set to 1 (i.e., the ideal solution model). The method suggested by Chung et al. [30] is employed

to calculate the viscosity of the gas mixture while the thermal conductivity is based on the group contribution model of Roy and Thodos [31,32]. The binary gas-phase mass diffusivity is calculated using the empirical model of Fuller et al. [33] with corrections for pressure effects using the Takahashi correlation [34]. For multi-component mixtures, the effective diffusivity is obtained using the formula given by Bird et al. [35]. The gas density is calculated directly from the PR-EOS [36], while the liquid–vapor equilibrium condition, including ϕ_k and L_k, is also computed directly from the PR-EOS (e.g., see Ref. [33]).

The enthalpy of the gas mixture is based on a molar weighting of the pure component enthalpies obtained from the CHEMKIN database (computed using the THERM software [37]). A generalized thermodynamic correlation based on a three-parameter corresponding states method [38] is used to compute the enthalpy correction for high-pressure effects. The specific internal energy of the gas mixture in Eq. (A4) is given by

$$I = \sum_{k=1}^{N} Y_k h_k(T) - P\upsilon \tag{A20}$$

which relates the specific internal energy to the equation of state through the gas temperature and pressure.

The liquid-phase properties are determined using the following. The heat capacity of pure component is calculated based on the group contribution model described by Rùzicka and Domalski [39] and then extended to mixtures (for the absorbed oxygen + diluent gases) using Filippov's rule [40]. The thermal conductivity and mass diffusivity are obtained using the correlations of Latini et al. [33] and Nakanishi [41], respectively. The density is calculated based on a fourth-order polynomial fit of experimental data [42], with these recorded near 1 atm, along with the high pressure correction given by Thomson et al. [43]. The viscosity is computed using a power law fit of experimental data near 1 atm [42].

A.6. Effects of thermodynamic non-equilibrium

To assess the influence of thermodynamic non-equilibrium behavior on the wet compression process at the conditions of interest for this study simulations are conducted where the sub-model described in Appendix A.2.2 is implemented in the wet compression software. *n*-Dodecane is used as the fuel with oxygen and nitrogen as the gas-phase species. An initial temperature and pressure of $T_0 = 350$ K and $P_0 = 1$ bar, respectively, are used at two droplet sizes, $d_0 = 3$ and 8 μm. In addition, a range of mass and thermal accommodation coefficients is explored. The initial Knudsen numbers are $Kn_0 = 0.02$ and 0.007 for these two droplets. K_n is computed here using $\eta^2 = (4D_{gf})^2/\pi v_{\text{rms}}^2$ where v_{rms} is the root mean squared velocity of the vaporized fuel at the droplet surface; this is taken to be proportional to $\sqrt{T_{l,rs}}$ based on kinetic theory.

The results for these simulations for $d_0 = 3$ μm condition are illustrated in Fig. A2. There is very little difference in overall evaporation behavior for the $d_0 = 8$ μm condition, which is consistent with other studies [21–23] which demonstrated that larger droplets are less affected by thermodynamic non-equilibrium conditions. In Fig. A2 the non-dimensional surface areas for the droplets are plotted as a function of time. The thermodynamic equilibrium results are compared to non-equilibrium conditions covering values of $\delta^m = 0.1$, 0.5 and 0.9, and $\delta^T = 0.1$, 0.5 and 0.9. It should be noted that accommodation coefficients are not well established in the literature (e.g., see Refs. [44–49]), but the values listed here cover the range found or utilized in most studies. In Fig. A2 it can be seen that the evaporation times are slightly more sensitive to values for δ^m than for δ^T, and that the influence of these parameters is non-linear. Overall, the change in total evaporation time is small, where this on the order of +5–10%; similar differences are seen for heavier hydrocarbons (e.g., *n*-hexadecane) while slightly greater discrepancies are seen for water droplets (e.g., 10–15%), as discussed in Ref. [26]. The temperature jump across the free-molecular region for the $\delta^T = 0.1$ case is on the order of 2–5 K through most of the droplet's lifetime; the jump is ~1 K for the $\delta^T = 0.9$ case.

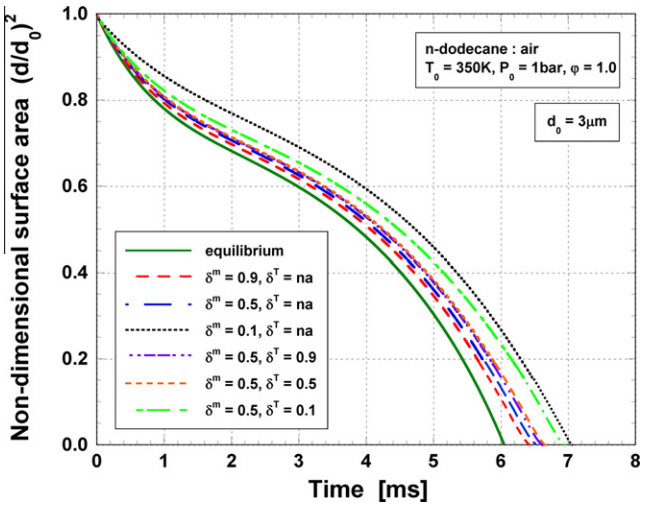

Fig. A2. Non-dimensional droplet surface areas as a function of time for various mass and thermal accommodation coefficients for *n*-dodecane in air using an initial temperature and pressure of $T_0 = 350$ K and $P_0 = 1$ bar at a droplet size of $d_0 = 3$ μm.

Based on these results it is concluded that the assumption of thermodynamic equilibrium at the droplet surface, for the purposes of this study is reasonable. However, design-representative calculations may benefit from the utilization of a non-equilibrium sub-model.

References

[1] S. Kimura, O. Aoki, Y. Kitahara, E. Aiyoshizawa, SAE Paper 2001-01-0200, 2001.
[2] H. Yanagihara, SAE Paper 2002-30-0009, 2002.
[3] H. Ogawa, N. Miyamoto, K. Akao, SAE 2002-08-0423, 2002.
[4] S. Simescu, S.B. Fiveland, L.G. Dodge, SAE 2003-01-0345, 2003.
[5] M. Canova, S. Midlam-Mohler, Y. Guezennec, G. Rizzoni, Int. J. Veh. Des. 44 (2007) 62–83.
[6] G.C. Martin, C.J. Mueller, D.M. Milam, M.S. Radovanovic, C.R. Gehrke, SAE 2008-01-2400, 2008.
[7] J.H. Mack, S.M. Aceves, R.W. Dibble, Energy 34 (2009) 782–787.
[8] M. Chaker, C.B. Meher-Homji, T. Mee III, J. Eng. Gas Turb. Power 126 (2004) 545–580.
[9] R. Bhargava, C.B. Meher-Homji, J. Eng, Gas Turb. Power 127 (2005) 145–158.
[10] R.K. Bhargava, C.B. Meher-Homji, M.A. Chaker, M. Bianchi, F. Melinao, A. Peretto, J. Eng. Gas Turb. Power 129 (2007) 454–472.
[11] J. Vanderover, M.A. Oehlschlaeger, Int. J. Chem. Kinet. 41 (2009) 82–91.
[12] K. Kumar, C.-J. Sung, Combust. Flame 157 (2010) 676–685.
[13] D.F. Davidson, D.R. Haylett, R.K. Hanson, Combust. Flame 155 (2008) 108–117.
[14] C. Allen, T. Lee, AIAA-2009-0227, 2009.
[15] G. Mittal, C.-J. Sung, Combust. Flame 145 (2006) 160–180.
[16] M.V. Johnson, G.S. Zhu, S.K. Aggarwal, S.S. Goldsborough, Int. J. Heat Mass Transfer 53 (2010) 1100–1111.
[17] G.S. Zhu, S.K. Aggarwal, Int. J. Heat Mass Transfer 43 (2000) 1157–1171.
[18] G.S. Zhu, R.D. Reitz, S.K. Aggarwal, Int. J. Heat Mass Transfer 44 (2001) 3081–3093.
[19] G.S. Zhu, S.K. Aggarwal, J. Eng, Gas Turb. Power 124 (2002) 762–770.
[20] W. Li, E.J. Davis, Aerosol Sci. Technol. 25 (1996) 11–21.
[21] S.S. Sazhin, I.N. Shishkova, A.P. Kryukov, V.Yu. Levashov, M.R. Heikal, Int. J. Heat Mass Transfer 50 (2007) 2675–2691.
[22] V.R. Dushin, A.V. Kulchitskiy, V.S. Nerchenko, V.F. Nikitin, E.S. Osadchaya, Yu.G. Phylippov, N.N. Smirnov, Acta Astronaut. 63 (2008) 1360–1371.
[23] S.S. Sazhin, I.N. Shishkova, Atom. Spray 19 (2009) 473–489.
[24] S.S. Goldsborough, C.J. Potokar, SAE Paper 2007-01-0169, 2007.
[25] S.M. Gallagher, H.J. Curran, W.K. Metcalfe, D. Healy, J.M. Simmie, G. Bourque, Combust. Flame 153 (2008) 316–333.
[26] S.S. Goldsborough, M.V. Johnson, G.S. Zhu and S.K. Aggarwal, Fuel, submitted for publication.

[27] C.K. Westbrook, W.J. Pitz, O. Herbinet, H.J. Curran, E.J. Silke, Combust. Flame 156 (2009) 181–199.
[28] V. Duprédurand, G. Castanet, F. Lemoine, Int. J. Heat Mass Transfer 53 (2010) 3495–3502.
[29] S.S. Goldsborough, Combust. Flame 156 (2009) 1248–1262.
[30] T.H. Chung, M. Ajlan, L.L. Lee, K.E. Starling, Ind. Eng. Chem. 27 (1988) 671–679.
[31] D. Roy, G. Thodos, Ind. Eng. Chem. Fundam. 7 (1968) 529–534.
[32] D. Roy, G. Thodos, Ind. Eng. Chem. Fundam. 9 (1970) 71–79.
[33] B.E. Poling, J.M. Prausnitz, J.P. O'Connell, The Properties of Gases and Liquids, 5th ed., 2001.
[34] S. Takahashi, J. Chem. Eng. 6 (1974) 417–420.
[35] R.B. Bird, W.E. Stewart, E.N. Lightfoot, Transport Phenomena, John Wiley and Sons, New York, 1960.
[36] D.Y. Peng, D.B. Robinson, Ind. Eng. Chem.: Fundam. 15 (1976) 59–64.
[37] E.R. Ritter, J.W. Bozzelli, Int. J. Chem. Kinet. 23 (1991) 767–778.
[38] I.L. Byung, G.K. Michael, AIChE J. 21 (1975) 510–527.
[39] V. Rùzicka, E.S. Domalski, J. Phys, Chem. Ref. Data 22 (1993) 597–619.
[40] L.P. Filippov, Chem. Abstr. 50 (1956) 8276.
[41] K. Nakanishi, Ind. Eng. Chem. Fundam. 17 (1978) 253–256.
[42] D.R. Caudwell, J.P.M. Trusler, V. Vesovic, W.A. Wakeham, Int. J. Thermophys. 25 (2004) 1572–9567.
[43] G.H. Thomson, K.R. Brobst, R.W. Hankinson, AIChE J. 28 (1982) 671–676.
[44] A. Morita, M. Sugiyama, H. Kameda, S. Koda, D.R. Hanson, J. Phys. Chem. B. 108 (2004) 9111–9120.
[45] A. Laaksonen, T. Vesala, M. Kulmala, P.M. Winkler, P.E. Wagner, Atmos. Chem. Phys. Discuss. 4 (2004) 7281–7290.
[46] M. Zientara, D. Jakubczyk, G. Derkachov, K. Kolwas, M. Kolwas, J. Phys. D.: Appl. Phys. 38 (2005) 1978–1983.
[47] P.M. Windler, A. Vrtala, R. Rudolf, P.E. Wagner, I. Riipinen, T. Vesala, K.E.J. Lehtinen, Y. Viisanen, M. Kulmala, J. Geophys. Res. 111 (2006) D19202.
[48] E.J. Davis, Atmos. Res. 82 (2006) 561–578.
[49] H.A. Michelsen, Appl. Phys. B. 94 (2009) 103–117.